Nonlinear Modular State-Space Modeling of Power-Electronics-Based Power Systems

Federico Cecati, *Student Member, IEEE*, Rongwu Zhu, *Member, IEEE*, Marco Liserre, *Fellow, IEEE*, and Xiongfei Wang, *Senior Member, IEEE*

***Abstract*—Power system state-space models are often constructed by interconnection of their subsystems (converters, distribution lines, and grid). The interconnection between *L-/LCL*-filtered converters with the distribution lines subsystems is often realized through a virtual resistor, because they both have the voltage as input, introducing inaccuracy. Moreover, the parameters variations influence not only the eigenvalues, but also the equilibrium point. In this case, the small-signal model has to be reevaluated around the new equilibrium point. For the computation of the equilibrium point, an additional method, e.g., power flow, is conventionally used. However, the variables computed with power flow (e.g., $\mathbf{P}$, Q, $\mathbf{V}$, and θ) do not always coincide with the state-space model variables, required for the linearization. Furthermore, the traditional power flow does not consider the influence of the voltage-source-converter control system on the grid equilibrium point. This article proposes a nonlinear grid model that does not need the virtual resistor to be interconnected. The proposed model can be used both for equilibrium point computation through the Newton–Raphson method, and it can be linearized around the computed equilibrium point for small-signal analyses. Simulations and experiments are provided.**

***Index Terms*—Control systems, nonlinear systems, power converter, power system modeling, power system stability, state-space methods.**

I. Introduction

THREE-PHASE voltage source converters (VSCs) are becoming the main actors in modern electric grids [1]–[4], leading to a substantial change also in the power system modeling and stability analysis approaches [5]–[8]. Eigenvalue small-signal analysis is a well-established tool to identify the natural frequency and damping ratio of the oscillatory modes in the grid [9], yet it requires a state-space model of the VSCs and the grid, which include all the dynamics relevant to the phenomena of interest [5], [6], [8], [10]–[14].

The VSC outer control loops (e.g., synchronization, power, and ac and dc voltage control) present a nonlinear behavior, and they all play a fundamental role in the power system low-frequency dynamics [5], [7], [15]. Several articles studied, at system level, the dynamics of phase-locked loop (PLL)-based VSCs [8], [10], [12], [16]–[19], or power synchronization-based VSCs [6], [7], [20]–[23]. The *LCL* filter and the digital delay dynamics are included in some models in literature [6], [7], [20], [24], [25], nevertheless Gu *et al.* [26] highlighted that in system-level low-frequency analyses, they can be neglected in order to keep the model order low, since they influence only the high-frequency dynamics. Once having the VSC models, the considered grid model is conventionally build through modular methodologies, which divide it into fundamental subsystems (VSCs, distribution lines, and ac grid) and interconnect them properly [7], [20], [25]. Yet, the strategies in literature to realize the interconnections present two limitations.

Considering *L-/LCL*-filtered VSCs as in [6], [7], [20], [24], [25], and [27], the voltages at each node of the network are treated as input variables both for the VSCs and the distribution lines subsystems, making the interconnection challenging [7]. The introduction of a virtual resistor was proposed in [7] and later used in [6], [20], [24], and [25] to break through this limit. Recently, Wang *et al.* [25] demonstrated that the value of the virtual resistor has a relevant influence on the power system dynamics, representing a potential source of inaccuracy.

Second, the model linearization process requires the knowledge of the equilibrium point [28]. Conventionally, the linearization is applied at the VSC level, and the grid small-signal model is build by merging the matrices of the linearized VSCs models [6], [7], [20], [24], [25]. However, the VSCs equilibrium points depend on the whole grid configuration and has to be computed at the power system level, as clear from the power flow theory [7], [29]. The conventional small-signal power system models are not adequate for equilibrium point computation, thus a separate nonlinear grid model, either a power flow or a numerical time-step simulation, is commonly built and employed for it [7]. On the one hand, numerical simulation models allow high VSC modeling flexibility, nevertheless they are slower than analytic models solved with Newton–Raphson (e.g., power flow) for steady-state computations [30]. On the other hand, the

Manuscript received September 20, 2021; accepted November 2, 2021. Date of publication November 12, 2021; date of current version January 19, 2022. This work was supported in part by the Gesellschaft für Energie und Klimaschutz Schleswig-Holstein GmbH (EKSH) doctoral studies grant, in part by the Deutsche Forschungsgemeinschaft (DFG, German Research Foundation) via the Priority Programme DFG SPP 1984 "Hybrid and Multimodal Energy Systems," and in part by the German Federal Ministry for Economic Affairs and Energy within the research project "Add-On" (0350022B). Recommended for publication by Associate Editor J. R. Espinoza. *(Corresponding author: Federico Cecati.)*

Federico Cecati and Marco Liserre are with the Chair of Power Electronics, University of Kiel, 24118 Kiel, Germany (e-mail: fc@tf.uni-kiel.de; liserre@ieee.org).

Rongwu Zhu is with the Harbin University of Technology, Shenzhen 518055, China (e-mail: rzh@hit.edu.cn).

Xiongfei Wang is with the Department of Energy Technology, Aalborg University, 9220 Aalborg, Denmark (e-mail: xwa@energy.aau.dk).

Color versions of one or more figures in this article are available at https://doi.org/10.1109/TPEL.2021.3127746.

Digital Object Identifier 10.1109/TPEL.2021.3127746

power flow in its classical formulation returns the steady-state values of P, Q, V, and θ at the grid buses, which does not always coincide with the variables in the state vector x of the state-space model, required for the linearization [28], [31], [32]. Moreover, conventional power flow models do not include the VSC control system, neglecting the influence of control parameters (e.g., ac voltage droop gain) or more advanced control schemes [18], [33] on the grid equilibrium point.

In this article, a nonlinear state-space model of a PLL-based VSC with dc voltage control is first derived and validated through simulations and experimental results. The latter model does not include the LCL filter fast dynamics and uses a novel current loop modeling strategy based on the state-space realization of its impedance model, aimed to make the interconnections without virtual resistor. Starting from the proposed VSC model, a modular methodology to build a nonlinear state-space model of a grid by interconnection of nonlinear subsystems is proposed, unlike [6], [20], [24], [25], and [27], which derive linearized power system models. Being nonlinear, the state-space model of the considered grid can be used for two purposes: for equilibrium point computation, by posing the state derivative null and solving it with Newton–Raphson, and for eigenvalue stability analysis, by linearizing it around the computed equilibrium point. Eigenvalue analyses are realized depending on the control loops gains and the active power levels, reevaluating the state-space model around the actual equilibrium point at each control gain and power level variation. Simulation and experimental results are carried out to validate the eigenvalue analyses.

The rest of this article is organized as follows. In Section II, the grid under consideration is presented. In Section III, the subsystems interconnection problem is addressed. Section IV deals with the linearization and Section V with the eigenvalue analyses. Section VI presents the simulations and Section VII the experimental results. Finally, Section VIII concludes this article.

II. System Description

The principle scheme of the considered three-phase grid following the VSC is depicted in Fig. 1(a). The current source $i_{\rm dc}$ represents the upstream energy source, e.g., photovoltaic panel or wind turbine. The voltage $v_{\rm dc}$ across the dc-link capacitor $C_{\rm dc}$ is controlled through a proportional-integral (PI) controller, the ac voltage v_g with a droop controller, and a synchronous reference frame PLL is implemented for the synchronization. The inner PI current loop regulates the converter output current i_g. The considered converter presents an L filter L_f but the argumentation can be extended also to *LCL*-filtered converters, neglecting the capacitor that influences only the high-frequency dynamics [34].

An arbitrary number n of VSCs as in Fig. 1(a) are connected to a grid by means of distribution lines with a resistive-inductive impedance Z_l, as shown in Fig. 1(b). The grid is modeled with a voltage source e in series with an *RL* impedance Z_g. The aim of this article is to propose a nonlinear modular modeling methodology, and apply it to a grid as in Fig. 1(b).

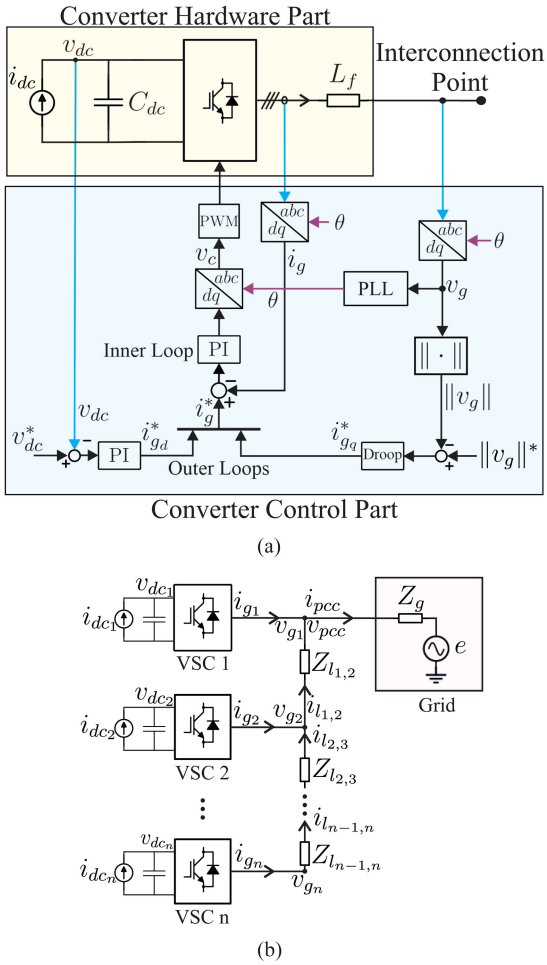

Fig. 1. (a) Considered grid-following three-phase voltage source converter in its hardware and control part. (b) Considered grid with n grid-following VSCs.

III. VSC Modeling and Subsystem Interconnection

Average models are often used in literature for the analysis of low-frequency dynamics on the dc and ac side [5]–[8], [20], [24], [34]. The digital delay and *LCL* filter influence only high-frequency dynamics, therefore, in this article, as in other articles, they are neglected [7], [26]. The modeling of the ac side and current control is crucial for the interconnection of the VSCs subsystems and the distribution lines subsystems, and is discussed in this section.

A. Traditional AC Side and Current Loop Modeling

The ac side of a VSC is often modeled in the state space with a dq voltage source v_c in series with the filter L_f, as in Fig. 2(a) [6], [7], [20], [24]–[27]. The transfer function $G_{\rm cc}(s) = K_p + \frac{K_i}{s}$ represents the PI current controller, and the term Ωi_g is the dq-axes decoupling term [34], considering

$$\Omega = \begin{pmatrix} 0 & -\omega \\ \omega & 0 \end{pmatrix} \tag{1}$$

with ω the fundamental grid angular frequency. The state-space model of the converter and its current loop as in Fig. 2(a), considering currents and voltages as vectors with d and q components,

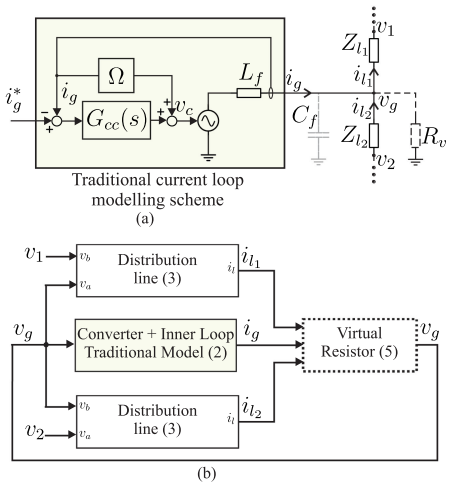

Fig. 2. Conventional state-space modeling of the VSC. (a) Modeling of the converter and its inner loop. (b) Interconnection with the power network through a virtual resistor.

e.g., $i_g = \begin{pmatrix} i_{g_d} \\ i_{g_q} \end{pmatrix}$, is

$$\begin{cases} \dot{i}_g = -\Omega i_g + \frac{1}{L_f}(v_c - v_g) \\ \dot{\Phi}_{\text{cc}} = i_g^* - i_g \\ v_c = K_p(i_g^* - i_g) + K_i \Phi_{\text{cc}} + L_f \Omega i_g \end{cases} \tag{2}$$

where Φ_{cc} is the integral state of the current error. The limitation of this model (2) arises when using it for the power system modeling. In (2), v_g is the disturbance input and i_g is the state/output variable, as in the block representation of Fig. 2(b). Analogously, distribution lines, modeled with *RL* branches, have the terminal voltages v_a and v_b as inputs and the flowing current i_l as state/output variables, as shown in Fig. 2(b)

$$\dot{i}_l = -\frac{R_l}{L_l} i_l - \Omega i_l + \frac{1}{L_l}(v_b - v_a). \tag{3}$$

The voltage v_g in the node, shown in Fig. 2(a), is an input variable both for the converter (2) and the distribution lines (3), as highlighted in Fig. 2(b), thus is difficult to obtain [7]. This problem exists when considering *L-/LCL* filtered VSC: with *LC* output filter as the gray dashed line in Fig. 2(a), v_g can be set as state variable with differential equation

$$\dot{v}_g = -\Omega v_g + \frac{1}{C_f}(i_g + i_{l_2} - i_{l_1}) \tag{4}$$

and used in (2) and (3). In case of the *L* filter, Pogaku *et al.* [7] proposed to add a virtual resistor R_v in the interconnection node, as in Fig. 2(a) and get the v_g expression as

$$v_g = R_v(i_g + i_{l_2} - i_{l_1}) \tag{5}$$

and substitute it into (2) and (3). It is important to notice that, when no capacitor in the VSC output filter is considered, v_g is *not* a state variable as in (4), rather an algebraic function of other variables as in (5). The interconnection through a virtual resistor is graphically represented in Fig. 2(b). An additional subsystem (virtual resistor) is added with the only target to realize the interconnection. Moreover, if R_v is chosen very high, the model may be bad-conditioned [30], if not high enough, it can introduce inaccuracy [25].

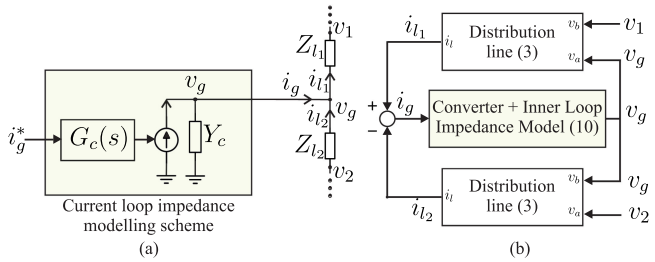

Fig. 3. Proposed state-space modeling of the VSC. (a) Modeling of the converter and its inner loop. (b) Interconnection with the power network.

B. AC Side Modeling Through an Inner Loop Impedance Model

Impedance-based modeling is often used in literature in the context of impedance-based stability analysis [15], [17], [35]–[37]. However, since it is based on transfer functions, it can be actually translated in state-space form and used for different aims. In this article, the converter and the current loop are modeled with the state-space representation of their impedance-based model, as shown in Fig. 3(a). In this way, a parallel admittance Y_c at the interconnection node is obtained, which allows the interconnection between VSCs and distribution lines without additional virtual resistors. The impedance model is derived with a procedure similar to [15], starting from (2) expressed in the dq Laplace domain, using the notation $\bar{v}_g = v_{g_d} + j v_{g_q}$ for the complex variables in the frequency domain.

$$\bar{i}_g = \frac{\bar{v}_c - \bar{v}_g}{L_f(s + j\omega)} \tag{6}$$

$$\bar{v}_c = (\bar{i}_g^* - \bar{i}_g)\left(K_p + \frac{K_i}{s}\right) + j\omega L_f \bar{i}_g. \tag{7}$$

By substituting (7) into (6), the impedance model of the VSC ac side with its current loop as in Fig. 3(a) is derived

$$\bar{i}_g = G_c(s)\bar{i}_g^* - Y_c(s)\bar{v}_g \quad \begin{cases} G_c(s) = \frac{K_p s + K_i}{L_f s^2 + K_p s + K_i} \\ Y_c(s) = \frac{s}{L_f s^2 + K_p s + K_i}. \end{cases} \tag{8}$$

In (8), $G_c(s)$ and $Y_c(s)$ both have two poles. The higher frequency pole, circa in $\frac{K_p}{L_f}$, is the bandwidth of the current controller, and will be denominated ω_{cc}. The other pole in $\frac{K_i}{K_p}$ is the inverse of the PI controller time constant [34]. In $G_c(s)$, the lower frequency pole cancels the zero in $\frac{K_i}{K_p}$ and only a low-pass filter with cut-off frequency ω_{cc} remains. In $Y_c(s)$, the higher frequency pole is neglected in order to obtain a first-order transfer function, which makes more straightforward the state-space representation. This assumption can be done since the current loop bandwidth is higher enough with respect to the frequency of the phenomena of interest. The extended demonstration can be found in [19]. Hence, the transfer functions

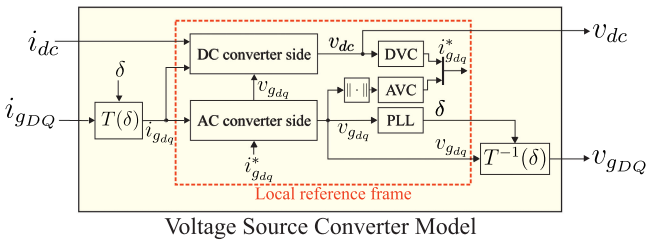

Fig. 4. Block graphical representation of the proposed model, including all its fundamental parts, and their interrelations.

in (8) become first order

$$\begin{cases} G_c(s) = \frac{\omega_{cc}}{s+\omega_{cc}} \\ Y_c(s) = \frac{s}{K_p s + K_i} \end{cases}. \tag{9}$$

Considering the approximation (9), by defining the non-physical variables $i_c = G_c(s) i_g^*$ and $v_{cc} = \frac{K_i}{s}(i_c - i_g)$, the impedance model (8) can be realized in a state-space form as

$$\begin{cases} v_g = K_p\,(i_c - i_g) + v_{cc} \\ \dot{v}_{cc} = K_i i_c - K_i i_g \\ \dot{i}_c = -\omega_{cc} i_c + \omega_{cc} i_g^* \end{cases}. \tag{10}$$

The obtained state-space model (10) is dynamically equivalent to the traditional model (2) but with different choices of state variables, in order to reverse the input/output pattern: i_g is a disturbance input and v_g is an output variable. This new input/output pattern is complementary to the one of the distribution lines, therefore the interconnection between VSC and distribution lines can be realized in a direct way without any additional virtual resistor, as shown in Fig. 3(b). However, also in the case of (10), v_g is *not* a state variable.

C. Complete VSC Modeling

The derived model of the ac side and inner loop (10) is embedded in the complete state-space model of the VSC according to Fig. 4, resulting in a nonlinear model [8], [20].

The importance of having a local dq and global DQ frame has been emphasized in [7], and is done through the matrix $T(\delta)$, e.g., $i_{g_{dq}} = T(\delta) i_{g_{DQ}}$, as highlighted in Fig. 4

$$T(\delta) = \begin{pmatrix} \cos\delta & \sin\delta \\ -\sin\delta & \cos\delta \end{pmatrix} \tag{11}$$

where δ is the angle between the VSC dq and the global DQ reference frame [7]. The dc-link voltage dynamics is described by the nonlinear power balance equation [34] as

$$\dot{v}_{\text{dc}} = -\frac{3}{2}\frac{1}{C_{\text{dc}}}\frac{v_{g_{dq}}^T T(\delta) i_{g_{DQ}}}{v_{\text{dc}}} + \frac{1}{C_{dc}} i_{\text{dc}}. \tag{12}$$

In order to assure the constant power source behavior, the dc current is set to $i_{\text{dc}} = \frac{P^*}{v_{\text{dc}}}$ with P^* the reference power. The PLL, dc-link, and ac voltage controller are modeled with three differential equations as follows:

$$\dot{\Phi}_{\text{dc}} = v_{\text{dc}} - v_{\text{dc}}^* \tag{13}$$

$$\dot{\delta} = \begin{pmatrix} 0 & K_{p,\text{PLL}} \end{pmatrix} v_g + K_{i,\text{PLL}} \Phi_q \tag{14}$$

$$\dot{\Phi}_q = \begin{pmatrix} 0 & 1 \end{pmatrix} v_g \tag{15}$$

and one algebraic equation for i_g^* as follows:

$$i_g^* = \begin{pmatrix} K_{p,\text{DC}}(v_{\text{dc}} - v_{\text{dc}}^*) + K_{i,\text{DC}}\Phi_{\text{dc}} \\ K_{p,\text{AC}}\left(v_g^* - \sqrt{v_g^T v_g}\right) \end{pmatrix} \tag{16}$$

where it yields $\sqrt{v_g^T v_g} = \|v_g\|$. Φ_{dc} and Φ_q are the integral states of the dc voltage control and the PLL, respectively.

By combining (10)–(16), the proposed nonlinear model of the VSC in the form

$$\begin{cases} \dot{x}_{\text{vsc}} = f_{\text{vsc}}(x_{\text{vsc}}, u_{\text{vsc}}) \\ y_{\text{vsc}} = h(x_{\text{vsc}}, u_{\text{vsc}}) \end{cases} \tag{17}$$

is obtained. The state of the VSC is defined in the local dq frame as

$$x_{\text{vsc}} = \begin{pmatrix} i_c & v_{\text{dc}} & \Phi_{\text{dc}} & \delta & \Phi_q & v_{\text{cc}} \end{pmatrix}^T \tag{18}$$

by omitting the subscript dq. The inputs and outputs, defined in the global DQ frame, are $u_{\text{vsc}} = \begin{pmatrix} i_{\text{dc}} & i_{g_{DQ}} \end{pmatrix}^T$ and $y_{\text{vsc}} = \begin{pmatrix} v_{\text{dc}} & v_{g_{DQ}} \end{pmatrix}^T$, as in Fig. 4.

The state equation $\dot{x}_{\text{vsc}} = f_{\text{vsc}}(x_{\text{vsc}}, u_{\text{vsc}})$ is

$$\begin{pmatrix} \dot{i}_c \\ \dot{v}_{\text{dc}} \\ \dot{\Phi}_{\text{dc}} \\ \dot{\delta} \\ \dot{\Phi}_q \\ \dot{v}_{\text{cc}} \end{pmatrix} = \begin{pmatrix} -\omega_{\text{cc}} i_c + \omega_{\text{cc}} i_g^* \\ -\frac{3}{2}\frac{1}{C_{\text{dc}}}\frac{v_g^T T(\delta) i_{g_{DQ}}}{v_{\text{dc}}} + \frac{1}{C_{\text{dc}}} i_{\text{dc}} \\ v_{\text{dc}} - v_{\text{dc}}^* \\ \begin{pmatrix} 0 & K_{p,\text{PLL}} \end{pmatrix} v_g + K_{i,\text{PLL}} \Phi_q \\ \begin{pmatrix} 0 & 1 \end{pmatrix} v_g \\ -K_i T(\delta) i_{g_{DQ}} + K_i i_c \end{pmatrix} \tag{19}$$

and the output equation $y_{\text{vsc}} = h_{\text{vsc}}(x_{\text{vsc}})$ is

$$\begin{pmatrix} v_{\text{dc}} \\ v_{gDQ} \end{pmatrix} = \begin{pmatrix} v_{\text{dc}} \\ T^{-1}(\delta) v_g \end{pmatrix}. \tag{20}$$

The voltage v_g is kept implicit in the model for compacted of notation, and is expressed according to (10) as

$$v_g = K_p\left(i_c - T(\delta) i_{g_{DQ}}\right) + v_{\text{cc}}. \tag{21}$$

The nonlinear model (19) does not include the *LCL* filter dynamics, having lower order than models that do [6], [7], [20], [24], [25], [27]. For low-frequency analyses, (19) can be used both for *L*- and *LCL*-filtered converters, neglecting the filter fast dynamics [26].

The fact that v_g is expressed through (21) and is not a state variable represents a challenge for the linearization and equilibrium point computation, discussed in the next section.

IV. Power System Modeling and Linearization

The conventional power systems state-space modeling procedure is described in Fig. 5 [6], [7], [20], [24]. The linearization process, highlighted in orange, is done at the VSC level. The matrices of the VSC linearized models are then merged together to construct the linearized state-space matrix of the grid, denominated $\mathbf{A_{ps}}$ [7], [25]. In order to realize small-signal analyses, the matrix $\mathbf{A_{ps}}$ has to be evaluated at the grid model equilibrium state, denominated $\mathbf{x_{ps}}_e$. The computation of $\mathbf{x_{ps}}_e$ requires a nonlinear model of the whole considered grid, as clear from the power flow theory [7], [29]. Since the procedure in Fig. 5 aims to obtain a small-signal model of the considered grid, a *separate* and *additional* nonlinear model of the same grid, either power

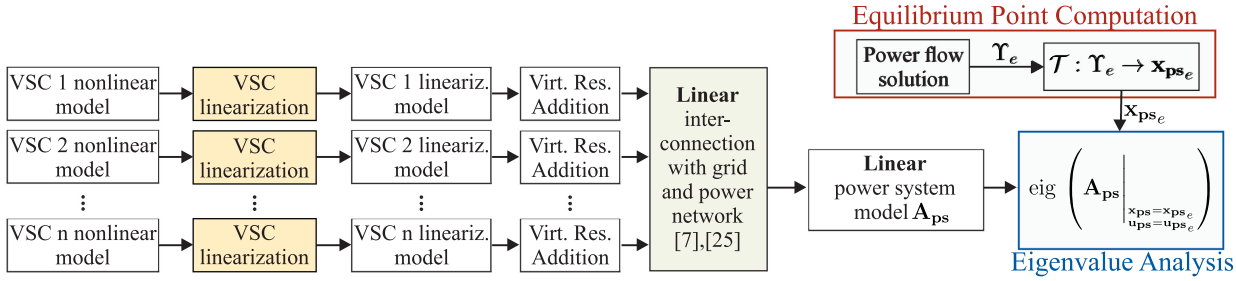

Fig. 5. Conventional methodology for the power system state-space model derivation, linearization, and eigenvalue analysis.

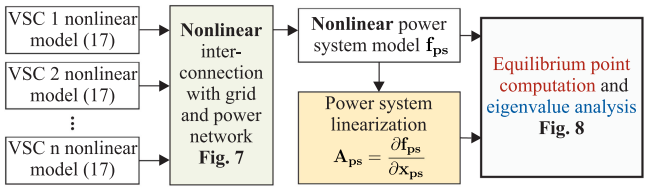

Fig. 6. Proposed methodology for the power system state-space model derivation, linearization, and eigenvalue analysis.

flow or a numerical time-domain simulation as proposed in [7], is usually employed to compute $\mathbf{x_{ps}}_e$, as shown in the red frame in Fig. 5. Numerical time-domain simulation models converge in many more steps than the power flow to the steady-state equilibrium point, thus are not considered in Fig. 5 [9], [29], [30].

On the other hand, the power flow in its classical formulation does not compute directly $\mathbf{x_{ps}}_e$, rather the steady-state values of $P, Q, V,$ and θ in the buses of the considered grid (denominated Υ_e in Fig. 5). From that, a function $\mathcal{T}: \Upsilon_e \rightarrow \mathbf{x_{ps}}_e$ to reconstruct $\mathbf{x_{ps}}_e$ starting from Υ_e has to be determined and used; such a function can sometimes be challenging to obtain. In our case, for example, the power flow variables V do not have a corresponding variable in $\mathbf{x_{ps}}_e$, since the voltages v_g of the VSCs are *not* state variables and are not contained in $\mathbf{x_{ps}}_e$ [28]. Furthermore, the traditional power flow does not contain the detailed VSCs control system model, which can have a relevant influence the grid equilibrium point.

This article proposes a modular methodology to built nonlinear power system state-space models by interconnection of the nonlinear VSCs models, as highlighted in Fig. 6. The resulting grid dynamic model has the form

$$\dot{\mathbf{x}}_{\mathbf{ps}} = \mathbf{f_{ps}}(\mathbf{x_{ps}}, \mathbf{u_{ps}}) \tag{22}$$

By considering null state derivative $\dot{\mathbf{x}}_{\mathbf{ps}} = \mathbf{0}$ (i.e., stationary state), and a constant input $\mathbf{u_{ps_e}}$, the differential equation (22) becomes an algebraic equation

$$\mathbf{f_{ps}}(\mathbf{x_{ps}}, \mathbf{u_{ps}}_e) = \mathbf{0}. \tag{23}$$

By solving (23) in $\mathbf{x_{ps}}$, the grid state-space model equilibrium point $\mathbf{x_{ps}}_e$ is directly obtained [28], [32]. The Newton–Raphson method can be used to efficiently solve (23), and requires the calculation of the Jacobian matrix $\frac{\partial}{\partial \mathbf{x_{ps}}}\mathbf{f_{ps}}$, as shown in orange in Fig. 6. The latter Jacobian matrix is exactly the state matrix $\mathbf{A_{ps}}$ of the grid small-signal state-space model obtained also in Fig. 5, whose eigenvalues describe the considered power system dynamics.

The novelty and unique feature of the proposed model (22) is that it can be used for *three* different purposes.

1) As a static algebraic equation for the equilibrium point computation [by numerically solving (23)].
2) As a small-signal model for eigenvalue analysis (from the Jacobian $\mathbf{A_{ps}} = \frac{\partial}{\partial \mathbf{x_{ps}}}\mathbf{f_{ps}}$).
3) As a dynamic differential equation (22) for time-domain simulations, as done in Section VI, by integrating the model over time

$$\mathbf{x_{ps}}(t) = \int_0^t \mathbf{f_{ps}}\left(\mathbf{x_{ps}}(\tau), \mathbf{u_{ps}}(\tau)\right)\, d\tau.$$

No additional power flow models has to be constructed and no functions $\mathcal{T}: \Upsilon_e \rightarrow \mathbf{x_{ps}}_e$ are needed, as shown in Figs. 5 and 6. Moreover, the detailed control system model is included in (23); the influence of the control loops (e.g., ac voltage droop) and potentially also more advanced control (e.g., virtual impedance, state-feedback control) on the equilibrium point is taken into account [18], [33].

A. *Derivation of the Nonlinear Power System Model* $\mathbf{f_{ps}}$

A power system composed of n parallel VSCs connected through distribution lines, as shown in Fig. 1(b), is considered. The fundamental steps for the nonlinear power system modeling are three, as shown in Fig. 7.

1) Step 1: VSCs Models Concatenation. The n nonlinear VSCs models are concatenated in a column vector, considering in each VSC $i_{\text{dc}} = \frac{P^*}{v_{\text{dc}}}$, obtaining

$$\begin{pmatrix} \dot{x}_{\text{vsc}_1} \\ \dot{x}_{\text{vsc}_2} \\ \vdots \\ \dot{x}_{\text{vsc}_n} \end{pmatrix} = \begin{pmatrix} f_{\text{vsc}_1}(x_{\text{vsc}_1}, \frac{P_1^*}{v_{\text{dc}_1}}, i_{g_1}) \\ f_{\text{vsc}_2}(x_{\text{vsc}_2}, \frac{P_2^*}{v_{\text{dc}_2}}, i_{g_2}) \\ \vdots \\ f_{\text{vsc}_n}(x_{\text{vsc}_n}, \frac{P_n^*}{v_{\text{dc}_n}}, i_{g_n}) \end{pmatrix} \tag{24}$$

$$\begin{pmatrix} v_{g_1} \\ v_{g_2} \\ \vdots \\ v_{g_n} \end{pmatrix} = \begin{pmatrix} h_{\text{vsc}_1}(x_{\text{vsc}_1}, i_{g_1}) \\ h_{\text{vsc}_2}(x_{\text{vsc}_2}, i_{g_2}) \\ \vdots \\ h_{\text{vsc}_n}(x_{\text{vsc}_n}, i_{g_n}) \end{pmatrix}. \tag{25}$$

The model of the n VSCs in (24) and (25) can be expressed in a compact form using a bold notation for the vectorial variables,

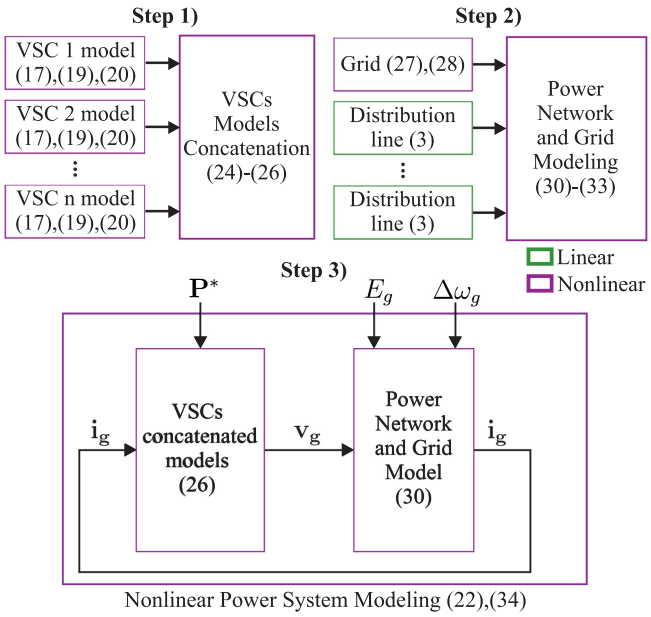

Fig. 7. Nonlinear interconnection procedure between VSCs, power network, and grid in three steps, described in Section IV-A.

e.g., $\mathbf{v_g} = (\, v_{g_1} \; v_{g_2} \; \cdots \; v_{g_n} \,)^T$, as

$$\begin{cases} \dot{\mathbf{x}}_{\mathbf{vsc}} = \mathbf{f_{vsc}}(\mathbf{x_{vsc}}, \frac{\mathbf{P}^*}{\mathbf{v_{dc}}}, \mathbf{i_g}) \\ \mathbf{v_g} = \mathbf{h_{vsc}}(\mathbf{x_{vsc}}, \mathbf{i_g}) \end{cases}. \tag{26}$$

2) Step 2: Power Network and Grid Modeling. The distribution lines are modeled as in (3). The grid is modeled with an ideal voltage source e with an RL impedance Z_g in series as in Fig. 1(b). The amplitude of the grid voltage is denominated E_g and its frequency deviation from the nominal value is denominated $\Delta\omega_g$. The global reference frame DQ is aligned with a virtual oscillator at the nominal frequency 50 Hz. A nonlinear operator $\Psi(E_g, \Delta\omega_g)$ is defined to transform the grid voltage expressed with amplitude E_g and frequency deviation $\Delta\omega_g$ into DQ coordinate frame:

$$\Psi : \begin{pmatrix} E_g \\ \Delta\omega_g \end{pmatrix} \rightarrow \begin{pmatrix} e_D \\ e_Q \end{pmatrix} = \begin{cases} \dot{\delta}_g = \Delta\omega_g \\ e_D = E_g \cos\delta_g \\ e_Q = E_g \sin\delta_g \end{cases} \tag{27}$$

through a frequency integration and a polar to Cartesian transformation. With this convention, a grid frequency drop of 1 Hz is seen as a clockwise rotation of the vector e_{DQ} at angular speed 2π rad/s.

The obtained Cartesian vector $e_{DQ} = \Psi(E_g, \Delta\omega_g)$ is then used in the equation of the RL branch obtaining

$$\dot{i}_{\mathrm{pcc}_{DQ}} = -\Omega i_{\mathrm{pcc}_{DQ}} - \frac{R_g}{L_g} i_{\mathrm{pcc}_{DQ}} + \frac{1}{L_g}(v_{\mathrm{pcc}_{DQ}} - e_{DQ}). \tag{28}$$

The state and the output of the power network model are defined, respectively, as

$$\mathbf{x_{net}} = \begin{pmatrix} i_{pcc} \\ i_{l_{1,2}} \\ \vdots \\ i_{l_{n-1,n}} \end{pmatrix} \qquad \mathbf{i_g} = \begin{pmatrix} i_{g_1} \\ i_{g_2} \\ \vdots \\ i_{g_n} \end{pmatrix} \tag{29}$$

and the derivation of its model is a well-known topic in the power system theory [9]. Considering the bold notation introduced in (26), the model is

$$\begin{cases} \dot{\mathbf{x}}_{\mathbf{net}} = \mathbf{A_{net}}\mathbf{x_{net}} + \mathbf{B_{net}}\mathbf{v_g} + \mathbf{F_{net}}\Psi(E_g, \Delta\omega_g) \\ \mathbf{i_g} = \mathbf{C_{net}}\mathbf{x_{net}} \end{cases} \tag{30}$$

with

$$\mathbf{A_{net}} = \begin{pmatrix} \frac{Z_g}{L_g} & 0 & \cdots & 0 \\ 0 & \frac{Z_{l_{1,2}}}{L_{l_{1,2}}} & \ddots & \vdots \\ \vdots & \ddots & \ddots & 0 \\ 0 & \cdots & 0 & \frac{Z_{l_{n-1,n}}}{L_{l_{n-1,n}}} \end{pmatrix} \tag{31}$$

$$\mathbf{B_{net}} = \begin{pmatrix} \frac{1}{L_g} & 0 & \cdots & 0 \\ -\frac{1}{L_{l_{1,2}}} & \frac{1}{L_{l_{1,2}}} & \ddots & \vdots \\ \vdots & \ddots & \ddots & 0 \\ 0 & \cdots & -\frac{1}{L_{l_{n-1,n}}} & \frac{1}{L_{l_{n-1,n}}} \end{pmatrix} \tag{32}$$

$$\mathbf{F_{net}} = \begin{pmatrix} -\frac{1}{L_g} \\ 0 \\ \vdots \\ 0 \end{pmatrix} \mathbf{C_{net}} = \begin{pmatrix} 1 & -1 & \cdots & 0 \\ 0 & \ddots & \ddots & \vdots \\ \vdots & & \ddots & -1 \\ 0 & \cdots & 0 & 1 \end{pmatrix}. \tag{33}$$

3) Step 3: Nonlinear Power System Modeling. The vector $\mathbf{v_g}$ defined in (26), which is the output of the VSCs, becomes the input of the power network in (30). In turn, the vector $\mathbf{i_g}$ defined in (30), which is the output of the power network, becomes input for the VSCs model in (26). The interconnection between the nonlinear VSCs model (26) and the power network (30) is thus realized. The resulting power system model has the active power levels of the VSCs $\mathbf{P}^*$ and the grid voltage E_g and frequency $\Delta\omega_g$ as input, and can be written as

$$\begin{pmatrix} \dot{\mathbf{x}}_{\mathbf{vsc}} \\ \dot{\mathbf{x}}_{\mathbf{net}} \end{pmatrix} = \begin{pmatrix} \mathbf{f_{vsc}}\left(\mathbf{x_{vsc}}, \frac{\mathbf{P}^*}{\mathbf{v_{dc}}}, \mathbf{C_{net}}\mathbf{x_{net}}\right) \\ \mathbf{A_{net}}\mathbf{x_{net}} + \mathbf{B_{net}}\mathbf{h}(\mathbf{x_{vsc}}, \mathbf{C_{net}}\mathbf{x_{net}}) + \mathbf{F_{net}}\Psi(E_g, \Delta\omega_g) \end{pmatrix}. \tag{34}$$

By defining $\mathbf{x_{ps}} = (\, \mathbf{x_{vsc}} \;\; \mathbf{x_{net}} \,)^T$ and $\mathbf{u_{ps}} = (\, \mathbf{P}^* \;\; E_g \;\; \Delta\omega_g \,))^T$, the model (34) can be written in a compact form as (22).

V. Linearization Point Computation and Eigenvalue Analysis

Eigenvalue analysis has been widely used in literature to analyze the effect of a parameter on the power system dynamical modes [6]–[9], [20], [24], [25], [27]. However, it is important to highlight that the variation of some parameters (e.g., the VSCs active power level, grid impedance, ac voltage droop gains) can change not only the power system dynamical modes, but also its steady-state equilibrium point $\mathbf{x_{ps}}_e$. In that case, the grid small-signal model needs to be reevaluated around its new

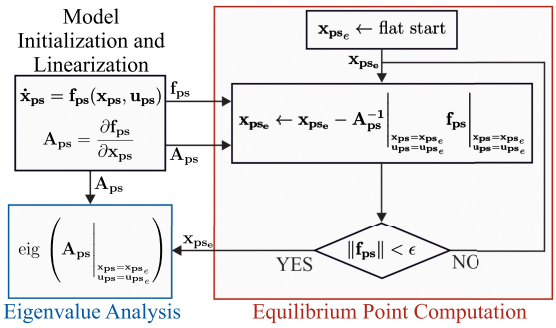

Fig. 8. Proposed eigenvalue analysis procedure with equilibrium point recomputation and update.

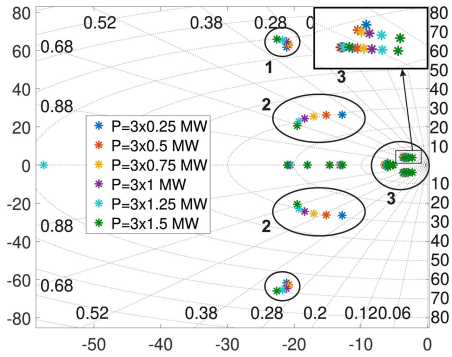

Fig. 9. Eigenvalue analysis of the considered power system with respect to VSCs power level variations.

equilibrium point. The proposed nonlinear model of the grid is operating point independent, and can be easily linearized around different operating conditions.

The procedure for that is shown in Fig. 8. The considered grid state-space model $\mathbf{f_{ps}}$ is initialized and its Jacobian matrix $\mathbf{A_{ps}}$ is derived, as already explained in Figs. 6 and 7 [9], [28], [32]. Both $\mathbf{f_{ps}}$ and $\mathbf{A_{ps}}$ are left parametric, in order to easily change their parameters during the stability analyses. The derivation of $\mathbf{A_{ps}}$ is not redone at each parameter variation, but only once in the initialization. Indeed, a parameter variation (active power or control gain) in the model without changes on the grid topology does not change the Jacobian matrix structure.

The equilibrium point can be computed by solving (23) with the Newton–Raphson iterative method, which needs the nonlinear system $\mathbf{f_{ps}}$ and its nonsingular Jacobian $\mathbf{A_{ps}}$, as represented in the red block in Fig. 8. By using as flat start in $\mathbf{x_{ps_e}}$ all $v_{\text{dc}} = v_{\text{dc}}^*$ and $v_{\text{cc}} = v_g^*$ and the other state variables posed to 0, the Newton–Raphson algorithm in Fig. 8 converged (on a laptop) on average in six iterations with precision 10^{-8} and an average execution time of 0.472 ms for each iteration. The Newton–Raphson convergence is clearly much faster than numerical time-domain transient simulations used by [7]. At the end of the Newton–Raphson iterations, the equilibrium point $\mathbf{x_{ps}}_e$ is available, and is substituted into the Jacobian matrix $\mathbf{A_{ps}}$ in order to realize the eigenvalue analysis, as shown in Fig. 8 in the blue frame.

A. Eigenvalue Analysis Depending on the VSCs Active Power

In Fig. 9, an eigenvalue analysis depending on the active power level is performed. The equilibrium point $\mathbf{x_{ps_e}}$ is recomputed at each power level variation, and the matrix $\mathbf{A_{ps}}$ reevaluated at the computed $\mathbf{x_{ps_e}}$, according to Fig. 8. The equilibrium values of the converters output voltages in their magnitude and angle are summarized in Table I. The grid impedance has a resistive component of 43 $m\Omega$ and inductive of 0.14 mH. The three VSCs are considered identical. Among the numerous eigenvalues of the considered grid, three groups that are relevant for the stability can be identified, as in Fig. 9. The group 1 represents an oscillatory mode at frequency around 70 Hz and is not particularly sensitive to the power level variations. The eigenvalue group 2 reveals an oscillatory dynamics at frequency around 30 Hz, whose damping decreases when the total injected power becomes low. Furthermore, a subsynchronous oscillatory mode due to the eigenvalue group 3 at frequency around 5 Hz arises when the total injected power increases toward 4.5 MW.

TABLE I
GRID EQUILIBRIUM POINT WITH RESPECT TO THE VSCS POWER LEVEL VARIATIONS INVESTIGATED IN FIG. 9

Power level	v_{g_1}	δ_1	v_{g_2}	δ_2	v_{g_3}	δ_3
$P = 3 \times 0.25$MW	571.73	0.10	579.39	0.12	583.02	0.13
$P = 3 \times 0.5$MW	575.60	0.20	587.84	0.23	593.37	0.25
$P = 3 \times 0.75$MW	576.49	0.29	591.01	0.34	597.14	0.36
$P = 3 \times 1$MW	575.47	0.38	590.40	0.44	596.07	0.46
$P = 3 \times 1.25$MW	573.29	0.46	586.95	0.53	591.24	0.56
$P = 3 \times 1.5$MW	570.48	0.56	581.30	0.62	583.37	0.66

The behavior of the latter group confirms the well-known results that with a high power level, with constant grid impedance, the short circuit ratio (SCR) decreases and the grid stability is threatened [7], [8]. On the other hand, this analysis reveals also that the active power injection has a positive damping effect on the eigenvalue group 2.

B. Eigenvalue Analysis Depending on the Outer Loops Parameters

Fig. 10 analyses the effect of dc-link control bandwidth, ac voltage droop gain, and PLL bandwidth on the considered power system low-frequency dynamics.

Also in this case, the three eigenvalues groups identified in Fig. 9 are present and directly influenced by the control loops parameters variations. The damping of the eigenvalues group 1 decreases when the dc-link controller bandwidth increases, decreases when the ac controller bandwidth increases, and is scarcely sensible of the PLL bandwidth. The group 2 is influenced by all the control loops: its damping increases when the dc-link voltage control bandwidth increases, increases when the ac voltage droop gain increases, and decreases when the PLL bandwidth increases. The group 3 presents a variable frequency, which is highly dependent on the PLL bandwidth; its frequency increases as the PLL bandwidth increases. Regarding the damping of this mode, it increases as the three parameters increase.

The steady-state values of the converters output voltages and angles are reported in Table II with respect to the different ac voltage droop gains considered in Fig. 10(b). When $K_{p,\text{AC}}$ is

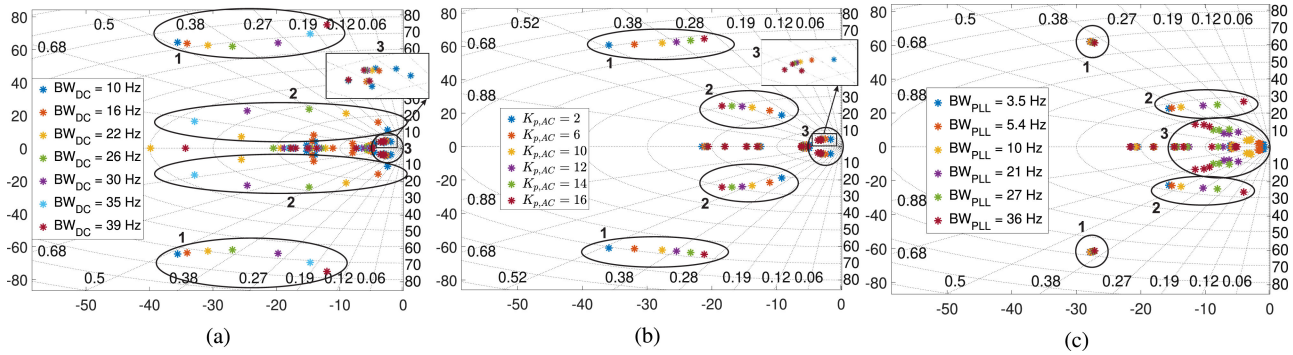

Fig. 10. Eigenvalue analyses of the considered power system with respect to control parameter variations. (a) DC-link voltage control bandwidth variation. (b) AC voltage droop gain variation. (c) PLL bandwidth variation.

TABLE II
GRID EQUILIBRIUM POINT WITH RESPECT TO THE AC VOLTAGE DROOP GAIN VARIATIONS INVESTIGATED IN Fig. 10(b)

$K_{p,AC}$	v_{g_1}	δ_1	v_{g_2}	δ_2	v_{g_3}	δ_3
$K_{p,AC}=2$	567.86	0.36	604.01	0.38	**621.66**	0.39
$K_{p,AC}=6$	556.06	0.38	584.41	0.41	597.65	0.42
$K_{p,AC}=10$	554.31	0.38	574.62	0.42	583.19	0.44
$K_{p,AC}=12$	554.93	0.39	571.25	0.42	577.45	0.45
$K_{p,AC}=14$	556.10	0.39	568.47	0.43	572.29	0.45
$K_{p,AC}=16$	557.64	0.39	566.10	0.43	567.56	0.45

low, the converters use less reactive current to compensate the voltage deviations. With $K_{p,\mathrm{AC}}=2$, the voltage v_{g_3} of the third converter becomes higher than 1.1 p.u. By increasing $K_{p,\mathrm{AC}}$, the reactive compensation by the converters bring the voltages closer to the nominal value. Interesting is to see the behavior of v_{g_1}, which decreases and goes away from the nominal value by increasing $K_{p,\mathrm{AC}}$. This is due to the high reactive power absorption by the VSCs 2 and 3, aimed to compensate their too high voltage levels, which affects also the voltage of the VSC 1. The results of this analysis confirm that the ac voltage droop gain has a high influence on the grid equilibrium point, and the model reevaluation around the new computed equilibrium point, as in Fig. 8, is a necessary operation.

The eigenvalue analyses performed in Sections V-A and V-B reveal that it does not exist a group of eigenvalues that is sensible only to one parameter variation, and all the dynamics are strongly coupled. This result stresses the fact that each control loop gives a fundamental contribution to the power system dynamics. In several analyses in literature, especially at power-system level, the dc-link voltage dynamics is neglected [7], [20], [24], [25], [27]. It is clear from Fig. 10(a) that as the dc-link voltage control bandwidth has a fundamental influence on the eigenvalues position, thus has to be included in the model.

VI. SIMULATION RESULTS

Time-domain simulations are performed to validate the proposed model and the eigenvalue analyses. The proposed VSC model (19)–(20) is used to model an *L*-filtered VSC-based wind turbine connected to the grid; the simulation parameters are summarized in Table III. A voltage sag is simulated, and the detailed switching VSC model is compared with the proposed nonlinear

TABLE III
VSC-BASED WIND TURBINE AND GRID SIMULATION PARAMETERS

Parameters	Values
Line-to-line grid voltage (V)	690
Short Circuit Ratio	2.6
R/X ratio	0.3
Power rating (MW)	2
DC-link voltage (V)	1100
Switching frequency (kHz)	2
DC-link capacitor (mF)	22
Filter inductor (mH)	0.1
DC-link voltage control bandwidth (Hz)	22
$K_{p,AC}$	10
PLL Bandwidth (Hz)	10

VSC model and the linearized small-signal model, to validate their accuracy. Afterwards, the eigenvalue analyses presented in Section V are validated through time-domain simulations.

A. VSC Nonlinear Model Validation

For the model validation, a grid as in Fig. 1(b) with a single VSC is considered ($n=1$). The ac voltages and currents are expressed in the dq frame aligned with the PCC voltage. The comparison with the detailed switching model is done on the basis of two different disturbances: a symmetrical voltage sag with 0.2-p.u. depth, shown in Fig. 11, and a frequency drop of 2 Hz, shown in Fig. 12. The small-signal model, included in the simulation, is computed from the nonlinear model as

$$\dot{\mathbf{x}}_{\mathbf{ps}} = \mathbf{f}_{\mathbf{ps}}(\mathbf{x}_{\mathbf{ps}_e}) + \mathbf{A}_{\mathbf{ps}}\left(\mathbf{x}_{\mathbf{ps}} - \mathbf{x}_{\mathbf{ps}_e}\right) + \mathbf{B}_{\mathbf{ps}}\left(\mathbf{u}_{\mathbf{ps}} - \mathbf{u}_{\mathbf{ps}_e}\right) \tag{35}$$

where $\mathbf{B}_{\mathbf{ps}} = \frac{\partial}{\partial \mathbf{u}_{\mathbf{ps}}}\mathbf{f}_{\mathbf{ps}}$ [28]. Both the simulations in Figs. 11 and 12 confirm the good faithfulness of the proposed nonlinear model with respect to the detailed switching model. High-frequency ripples, which are present in the detailed switching model in Figs. 11 and 12, are due to the power semiconductors devices switching. The proposed nonlinear model is an average model, therefore, it captures only the low-frequency behavior of the converter. Indeed, the high-frequency ripples are not present. The small-signal model has different behaviors in the two simulations of Figs. 11 and 12. In Fig. 11, the dynamics in the transient is not far from the nonlinear model, nevertheless there is a steady-state error after the sag, due to the fact that

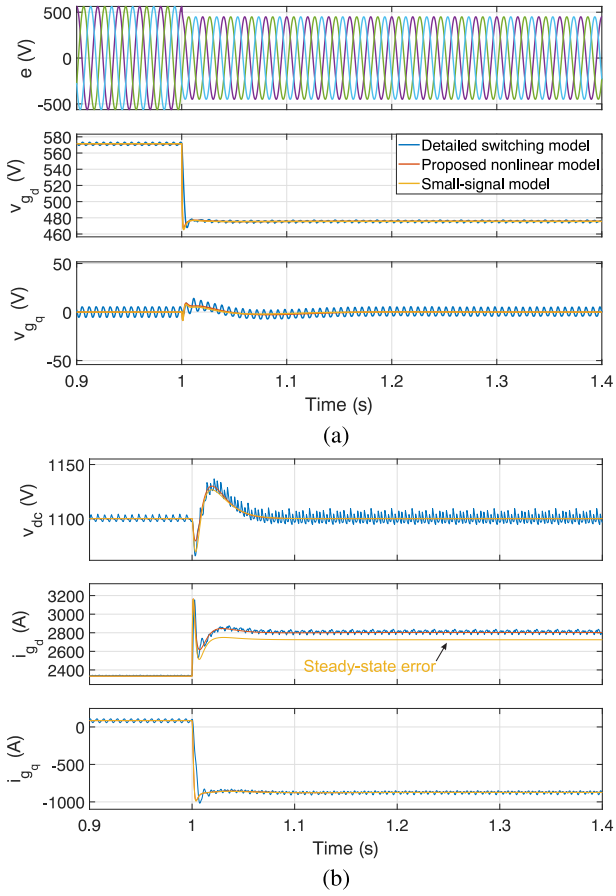

Fig. 11. Simulation of a voltage sag. (a) Three-phase grid voltage and the PCC voltage. (b) DC-link voltage and the ac current.

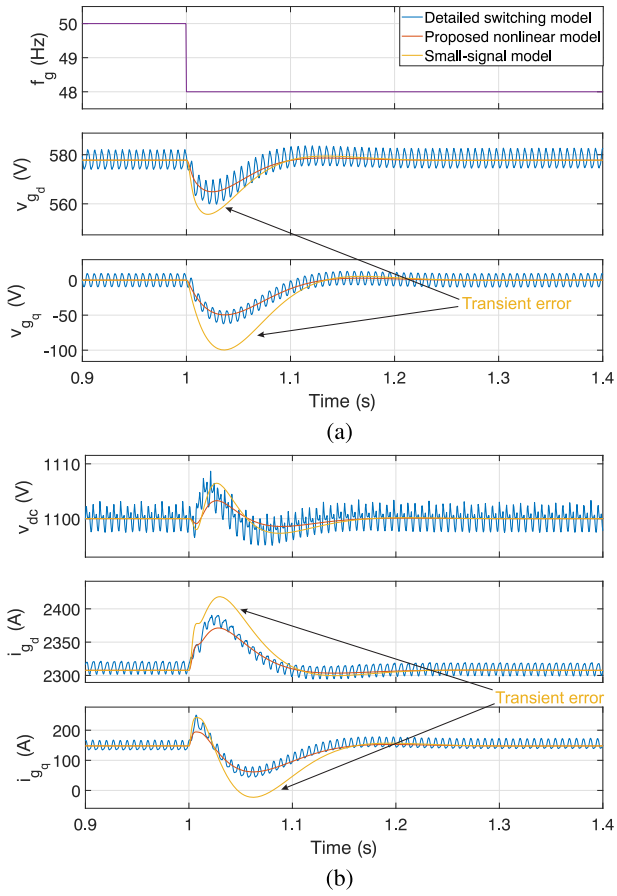

Fig. 12. Simulation of a frequency dip. (a) Grid frequency and the PCC voltage. (b) DC-link voltage and the ac current.

the model is linearized around the presag operating point. On the other end, in the simulation of the frequency sag of Fig. 12, the transient behavior is not accurately predicted by the small-signal model. Indeed, the transformation matrix $T(\delta)$ defined in (11), which rotates the converter reference frame during frequency events, is nonlinear, and its linearization can be inaccurate when δ deviates from its equilibrium point, such as during frequency events.

B. Simulation of Different Power Level in the VSCs

The reaction of the considered grid to a voltage sag depending on the active power levels of the VSCs is depicted in Fig. 13. A system as in Fig. 1(b) with three VSCs ($n = 3$) is now considered, as in the analysis in Fig. 9. When the power of each VSC is 0.25 MW, a higher frequency oscillatory behavior can be noticed, which is dependent on the eigenvalues of group 2 in Fig. 9, with frequency 25 Hz, which encounter a decrease of the damping when the power level decreases. On the other hand, another low-frequency oscillatory phenomena can be seen in Fig. 13, more evident on the current i_{pcc}; that is due to the eigenvalues in the group 3 of Fig. 9, with frequency around 4 Hz, which approach the imaginary axis when the power level increases. The presented simulation is, therefore, in agreement with the corresponding eigenvalue analysis of Fig. 9.

C. Simulation of Different Control Loop Parameters in the VSCs

In Fig. 14, the reaction of the considered grid to a voltage sag with different dc-link voltage controller bandwidths is depicted. For low bandwidths, the grid presents low-frequency oscillations with low damping. These oscillations are due to the eigenvalues in the groups 2 and 3 of Fig. 10(a), which approach the imaginary axis with low controller bandwidths. On the other hand, with high values of the control bandwidth, higher frequency oscillations arise, which derive from the eigenvalues group 1 in Fig. 10(a).

In Fig. 15, the simulation is performed under different values of the ac voltage droop gain. For low bandwidths, low-frequency oscillations with low damping arise, mostly due to the eigenvalues of the group 3 in Fig. 10(b). However, these oscillations are more damped with respect to the case of Fig. 14, since the eigenvalues of the group 2 in Fig. 10(a) are much more critical than the ones in Fig. 10(b). When the ac droop gain increases, higher frequency oscillations due to the eigenvalue group 1 in Fig. 10(b) arise. These oscillations are more damped and slightly slower with respect to the ones in Fig. 14(b) in accordance with the eigenvalue analyses in Fig. 10.

Ultimately, the simulation of the considered grid under different PLL bandwidths is shown in Fig. 16. With low bandwidths,

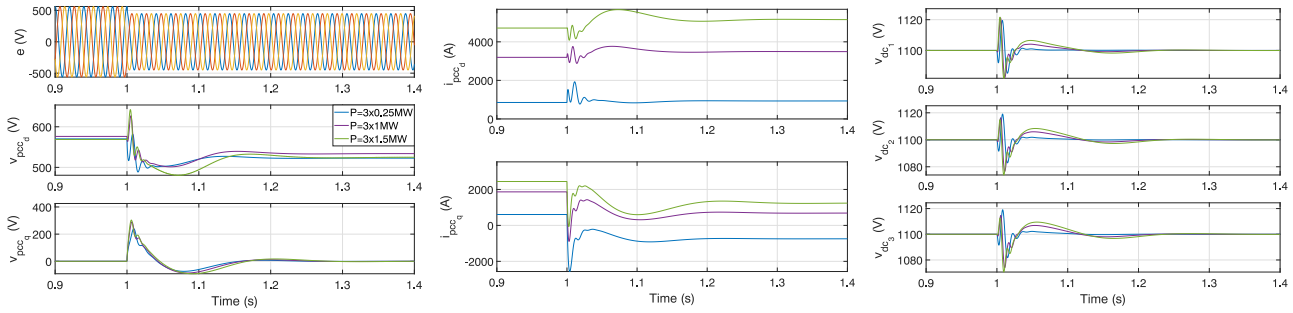

Fig. 13. Simulation under different VSCs power levels. (a) Grid voltage sag and the PCC voltage. (b) PCC current. (c) DC-link voltages of the three converters.

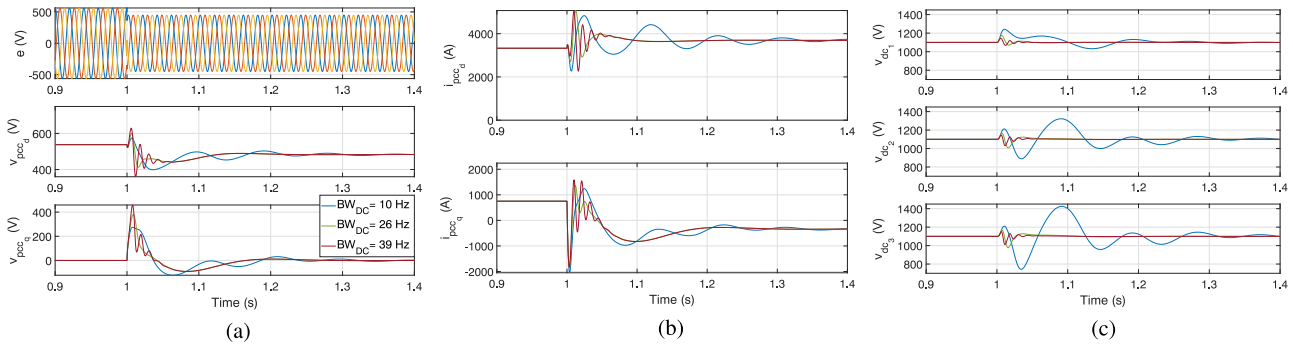

Fig. 14. Simulation under different dc-link voltage control bandwidths. (a) Grid voltage sag and the PCC voltage. (b) PCC current. (c) DC-link voltages of the three converters.

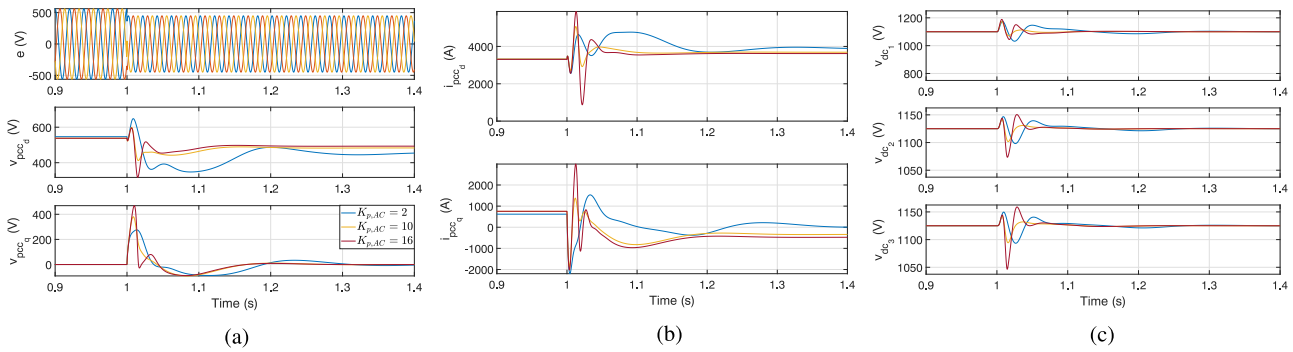

Fig. 15. Simulation under different ac voltage droop gain. (a) Grid voltage sag and the PCC voltage. (b) PCC current. (c) DC-link voltages of the three converters.

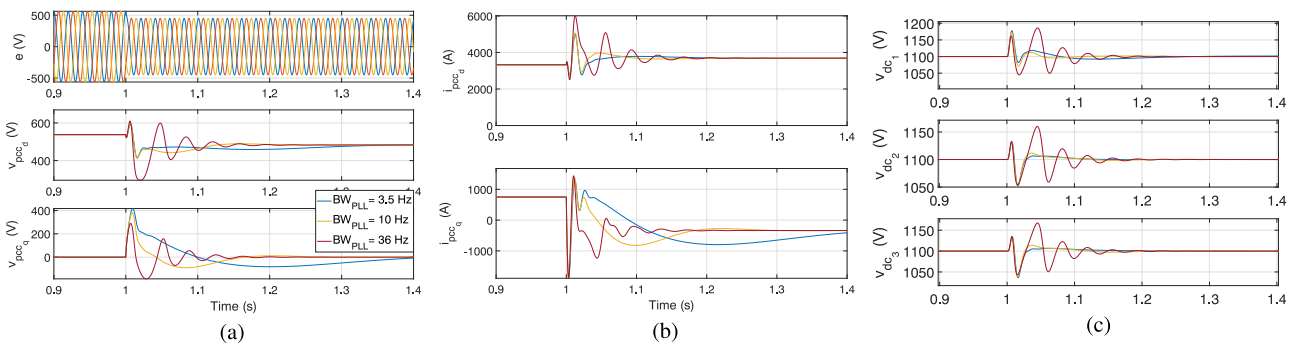

Fig. 16. Simulation under different PLL bandwidths. (a) Grid voltage sag and the PCC voltage. (b) PCC current. (c) DC-link voltages of the three converters.

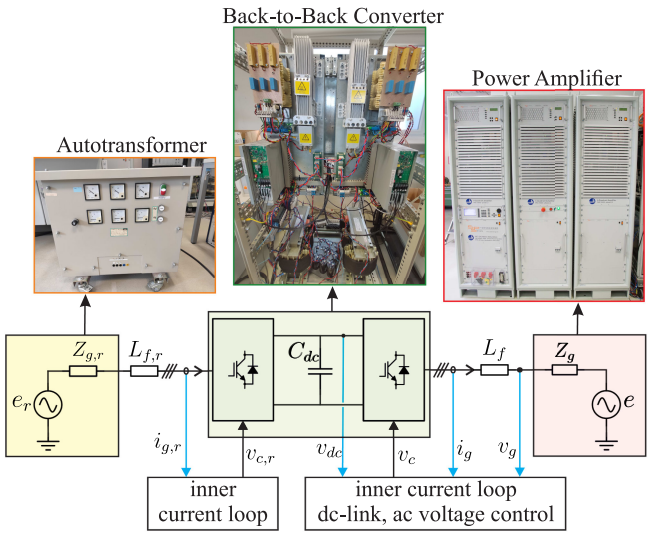

Fig. 17. Schematic of the setup used for the experimental results.

TABLE IV
BACK-TO-BACK CONVERTER AND POWER AMPLIFIER EXPERIMENTAL SETUP PARAMETERS

Parameters	Values
Line-to-line power amplifier voltage (V)	430
Power amplifier inductance Z_g (mH)	5.4
R/X ratio	0.3
Power rating (kW)	4
DC-link voltage (V)	600
Switching frequency (kHz)	10
DC-link capacitor (mF)	1.2
Filter inductor L_f (mH)	5.5

TABLE V
EXPERIMENTAL VALIDATION PARAMETERS

	Case study		
Parameters	1	2	3
Injected active power (kW)	1.8	2	1.6
DC-link voltage controller bandwidth (Hz)	12	36.2	18.3
AC voltage droop gain	0.12	0.7	0.4
PLL bandwidth (Hz)	4.9	16.4	5.9

the settling time of the voltages and currents is relatively long, nevertheless the oscillations are less prominent than Figs. 14 and 15. This is due to the eigenvalues of the group 3 of Fig. 10(c), which have a very low-frequency but higher damping when the PLL bandwidth is low. When the PLL bandwidth increases, low damped oscillations arise, as shown in Fig. 16. These oscillations are much slower with respect to the ones in Figs. 14 and 15. That is because they derive from group 2 in Fig. 10(c), which has significantly lower frequency with respect to group 1 in Fig. 10(a) and (b) responsible for the oscillations in Figs. 14 and 15.

VII. EXPERIMENTAL VALIDATION

The analyses and the simulations shown in the previous sections are based on the proposed VSC nonlinear model (19)–(20). The aim of this section is to experimentally validate the accuracy and effectiveness of the aforementioned nonlinear model through several case studies. The validation is carried out with respect to two different systems: a down-scaled experimental setup built in the lab, represented in Fig. 17, and a Typhoon Hardware-In-the-Loop (HIL) 402 real-time device.

A. Experimental Setup Tests

The VSC-based wind turbine system described in Section VI is reproduced in the lab through two converters connected in back-to-back configuration, as in Fig. 17. The right converter of the back-to-back corresponds to the grid-side converter of the wind turbine, and is the one represented in Fig. 1(a) and modeled by (19) and (20). This converter is plugged to a power amplifier by means of an inductive impedance Z_g, in order to emulate the grid. The left converter of the back-to-back is the generator-side converter, which emulates the wind turbine. This converter is modeled in Fig. 1(a) and in (19) and (20) as the current source $i_{\rm dc}$. It is connected to an autotransformer, as shown in Fig. 17, and controlled in current. The parameters of the setup used for the experiments are summarized in Table IV.

The experimental validation is realized as follows: a voltage sag of 0.35 p.u. is performed in the power amplifier and dc-link voltage, ac voltage and ac current of the VSC are recorded through an oscilloscope for three different case studies, summarized in Table V. The waveforms obtained from the oscilloscope in the three cases are depicted in Fig. 18; each case is compared with a simulation of the proposed nonlinear model (19)–(20) as shown in Fig. 19. The same control parameters are used in the experimental test and the corresponding nonlinear model simulation. Since the proposed model is entirely in the dq frame, a Park transformation is applied to the current i_g and voltage v_g, in order to obtain sinusoidal waveforms as in Fig. 19 and better compare them with the experimental results of Fig. 18. Being the system symmetrical and balanced, only one phase of v_g and i_g is displayed in Figs. 18 and 19.

The results in Figs. 18 and 19 highlight in all the three cases the high accuracy and good faithfulness of the proposed model with respect to the real model.

Moreover, the results are in accordance with the eigenvalue analyses of Figs. 9 and 10 as well. The case study (a), shown in Figs. 18(a) and 19(a), presents slower oscillations with respect to the other cases. By looking at Table V, it can be seen that the dc-link voltage control and the ac voltage droop gain are significantly minor with respect to the other cases. By looking at Fig. 10(a) and (b), it can be seen that the eigenvalues of the group 3, which have very low frequency, become less damped when there parameters decrease. The eigenvalues group 2 in Fig. 10(a) have also very low-frequency and damping values when the dc-link bandwidth decreases.

The case study (b) shown in Figs. 18(b) and 19(b) presents contrariwise faster oscillations with respect to the other cases. The control parameters used in this test, described in Table V, are higher with respect to the previous case. By looking at Fig. 10, the eigenvalues group 3, which has extremely low frequency, increases the damping when the three control loops parameters increase. On the other hand, in the case of the PLL, whose bandwidth in the case study (b) of Table V is more than three

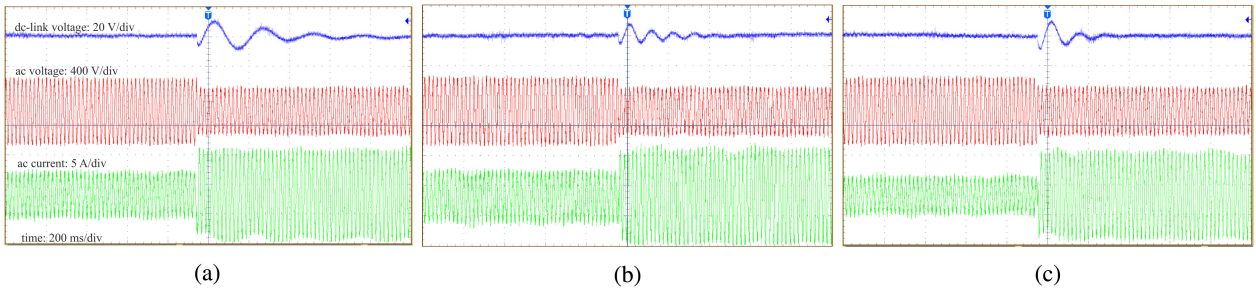

Fig. 18. DC-voltage dynamics in the experimental setup as a consequence of a voltage sag. (a) Case study 1. (b) Case study 2. (c) Case study 3.

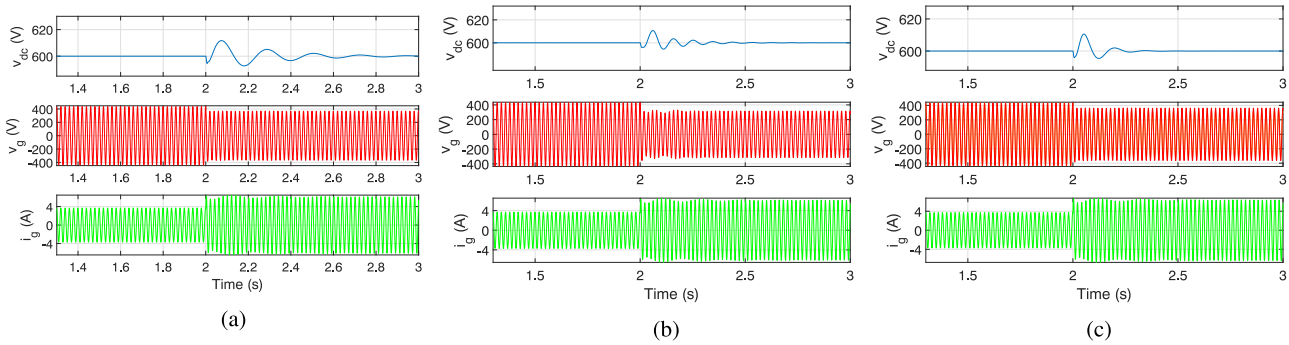

Fig. 19. DC-voltage dynamics in the simulation of the proposed nonlinear model as a consequence of a voltage sag. (a) Case study 1. (b) Case study 2. (c) Case study 3.

times higher than in case study (a), the eigenvalues group 2 has a responsibility for the observed oscillations, since its damping decreases when the PLL bandwidth increases. Moreover, also the eigenvalues of the group 1 in Fig. 10(a) and (b), which have a relatively high frequency, decrease their damping when the parameters increase.

The last case is shown in Figs. 18(c) and 19(c). The values of the three control loops parameters are in between the values of cases (a) and (b) described in Table V. The results is a system with more damped oscillations with respect to Fig. 18(a) and (b), and with a oscillation frequency, which is in between cases (a) and (b).

B. HIL Tests

A back-to-back VSC-based wind turbine system connected to the grid, with the same configuration depicted in Fig. 17, is modeled on a Typhoon HIL402 device. The HIL real-time simulation time step is 1 μs, which ensures accurate and realistic results for a converter with switching frequency of 2 kHz. The system parameters are summarized in Table III. A voltage sag of 0.2 p.u. with a simultaneous frequency dip of 1 Hz is simulated, and the virtual oscilloscope is triggered in the instant of the fault, capturing dc and ac voltage and ac current, as in Fig. 20(a). The proposed nonlinear model (19)–(20) and the small-signal model in the form (35) are both simulated, and their behavior is compared with the HIL results in Fig. 20(b). Being the state-space models expressed in the dq frame, the comparison has been done with the currents and voltages in the dq frame of the HIL model, given to the oscilloscope as internal signals of the VSC control system. The results in Fig. 20(b) are coherent with the simulation results in Section VI. The proposed nonlinear model shows a good faithfulness with the HIL results. The small-signal model behaves similarly to the real system, but it presents steady-state and transient errors due to the linearization, as discussed in Section VI.

VIII. Conclusion

In this article, a VSC modeling strategy is proposed, which does not include the *LCL* filter and allows the interconnection with the distribution lines subsystems without the virtual resistor. From that, a modular methodology to derive analytic nonlinear power system state-space models is presented. The obtained nonlinear state-space model is used for three purposes.

1) Steady-state equilibrium point computation, by means of the Newton–Raphson method. The proposed model contains the detailed model of the control system, and allows to analyze the influence of the control parameters on the grid equilibrium point.
2) System-level eigenvalue analysis, by recomputing the grid equilibrium point and reevaluating the model at the computed equilibrium point at each parameter change.
3) Nonlinear time-domain simulations, used to study the response of the considered grid to voltage and frequency events.

The eigenvalue, simulations, and experimental results highlight that both the control loops parameters of the VSCs and their power levels have a significant influence on the power system stability and equilibrium point, and are strongly coupled.

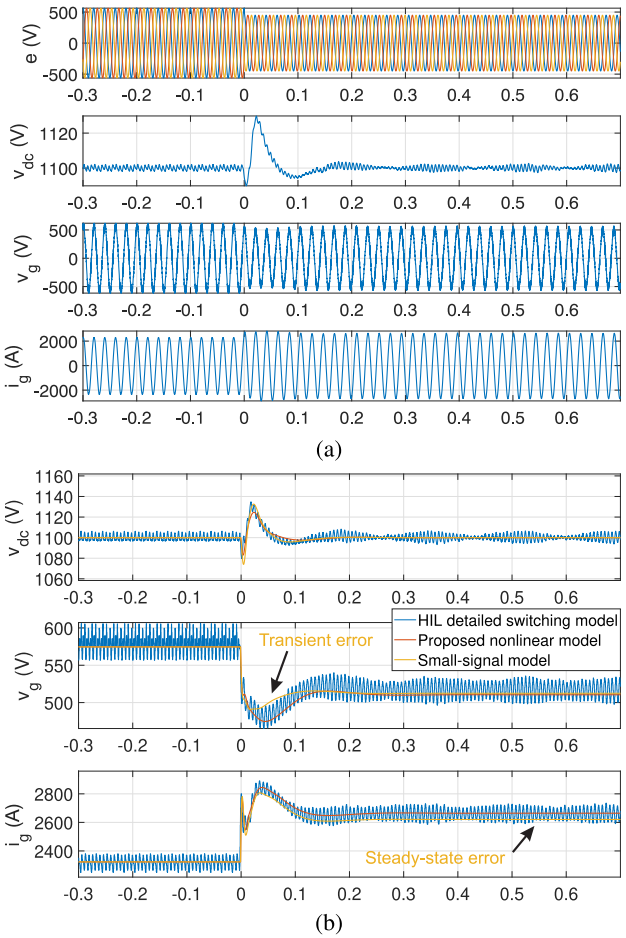

Fig. 20. Hardware-in-the-Loop (HIL) test of a voltage sag with frequency dip. (a) HIL results. (b) Comparison of the HIL results with the nonlinear and linearized model.

This dynamics coupling leads to a change in the way VSCs are modeled for power system studies: the inner structure dissolves and only the current/voltage characteristic at the outer ac and dc terminals remains.

REFERENCES

[1] F. Blaabjerg, Z. Chen, and S. B. Kjaer, "Power electronics as efficient interface in dispersed power generation systems," *IEEE Trans. Power Electron.*, vol. 19, no. 5, pp. 1184–1194, Sep. 2004.

[2] L. Gyugyi, "Unified power-flow control concept for flexible AC transmission systems," *Proc. IEE*, vol. 139, no. 4, pp. 323–331, Jul. 1992.

[3] M. Aneke and M. Wang, "Energy storage technologies and real life applications—A state of the art review," *Appl. Energy*, vol. 179, pp. 350–377, 2016.

[4] J. Rocabert, A. Luna, F. Blaabjerg, and P. Rodríguez, "Control of power converters in AC microgrids," *IEEE Trans. Power Electron.*, vol. 27, no. 11, pp. 4734–4749, Nov. 2012.

[5] X. Wang and F. Blaabjerg, "Harmonic stability in power electronic-based power systems: Concept, modeling, and analysis," *IEEE Trans. Smart Grid*, vol. 10, no. 3, pp. 2858–2870, May 2019.

[6] N. Bottrell, M. Prodanovic, and T. C. Green, "Dynamic stability of a microgrid with an active load," *IEEE Trans. Power Electron.*, vol. 28, no. 11, pp. 5107–5119, Nov. 2013.

[7] N. Pogaku, M. Prodanovic, and T. C. Green, "Modeling, analysis, and testing of autonomous operation of an inverter-based microgrid," *IEEE Trans. Power Electron.*, vol. 22, no. 2, pp. 613–625, Mar. 2007.

[8] Y. Huang, X. Yuan, J. Hu, and P. Zhou, "Modeling of VSC connected to weak grid for stability analysis of DC-link voltage control," *IEEE J. Emerg. Sel. Topics Power Electron.*, vol. 3, no. 4, pp. 1193–1204, Dec. 2015.

[9] P. Kundur, N. J. Balu, and M. G. Lauby, *Power System Stability and Control*. New York, NY, USA: McGraw-Hill, 1994.

[10] D. Dong, B. Wen, D. Boroyevich, P. Mattavelli, and Y. Xue, "Analysis of phase-locked loop low-frequency stability in three-phase grid-connected power converters considering impedance interactions," *IEEE Trans. Ind. Electron.*, vol. 62, no. 1, pp. 310–321, Jan. 2015.

[11] X. Zhang, D. Xia, Z. Fu, G. Wang, and D. Xu, "An improved feedforward control method considering PLL dynamics to improve weak grid stability of grid-connected inverters," *IEEE Trans. Ind. Appl.*, vol. 54, no. 5, pp. 5143–5151, Sep./Oct. 2018.

[12] C. Zhang, X. Wang, and F. Blaabjerg, "Analysis of phase-locked loop influence on the stability of single-phase grid-connected inverter," in *Proc. IEEE 6th Int. Symp. Power Electron. Distrib. Gener. Syst.*, 2015, pp. 1–8.

[13] Y. Huang and D. Wang, "Effect of control-loops interactions on power stability limits of VSC integrated to AC system," *IEEE Trans. Power Del.*, vol. 33, no. 1, pp. 301–310, Feb. 2018.

[14] D. Yang and X. Wang, "Unified modular state-space modeling of grid-connected voltage-source converters," *IEEE Trans. Power Electron.*, vol. 35, no. 9, pp. 9702–9717, Sep. 2020.

[15] L. Harnefors, M. Bongiorno, and S. Lundberg, "Input-admittance calculation and shaping for controlled voltage-source converters," *IEEE Trans. Ind. Electron.*, vol. 54, no. 6, pp. 3323–3334, Dec. 2007.

[16] F. Blaabjerg, R. Teodorescu, M. Liserre, and A. V. Timbus, "Overview of control and grid synchronization for distributed power generation systems," *IEEE Trans. Ind. Electron.*, vol. 53, no. 5, pp. 1398–1409, Oct. 2006.

[17] X. Wang, F. Blaabjerg, and W. Wu, "Modeling and analysis of harmonic stability in an AC power-electronics-based power system," *IEEE Trans. Power Electron.*, vol. 29, no. 12, pp. 6421–6432, Dec. 2014.

[18] F. Cecati, R. Zhu, M. Liserre, and X. Wang, "State-feedback-based low-frequency active damping for VSC operating in weak-grid conditions," in *Proc. IEEE Energy Convers. Congr. Expo.*, 2020, pp. 4762–4767.

[19] F. Cecati, R. Zhu, M. Langwasser, M. Liserre, and X. Wang, "Scalable state-space model of voltage source converter for low-frequency stability analysis," in *Proc. IEEE Energy Convers. Congr. Expo.*, 2020, pp. 6144–6149.

[20] M. Rasheduzzaman, J. A. Mueller, and J. W. Kimball, "Reduced-order small-signal model of microgrid systems," *IEEE Trans Sustain. Energy*, vol. 6, no. 4, pp. 1292–1305, Oct. 2015.

[21] Q. Zhong and G. Weiss, "Synchronverters: Inverters that mimic synchronous generators," *IEEE Trans. Ind. Electron.*, vol. 58, no. 4, pp. 1259–1267, Apr. 2011.

[22] O. Mo, S. D'Arco, and J. A. Suul, "Evaluation of virtual synchronous machines with dynamic or quasi-stationary machine models," *IEEE Trans. Ind. Electron.*, vol. 64, no. 7, pp. 5952–5962, Jul. 2017.

[23] L. Zhang, L. Harnefors, and H.-P. Nee, "Power-synchronization control of grid-connected voltage-source converters," *IEEE Trans. Power Syst.*, vol. 25, no. 2, pp. 809–820, May 2010.

[24] M. Rasheduzzaman, J. A. Mueller, and J. W. Kimball, "An accurate small-signal model of inverter- dominated islanded microgrids using *dq* reference frame," *IEEE J. Emerg. Sel. Topics Power Electron.*, vol. 2, no. 4, pp. 1070–1080, Dec. 2014.

[25] Y. Wang, X. Wang, Z. Chen, and F. Blaabjerg, "Small-signal stability analysis of inverter-fed power systems using component connection method," *IEEE Trans. Smart Grid*, vol. 9, no. 5, pp. 5301–5310, Sep. 2018.

[26] Y. Gu, N. Bottrell, and T. C. Green, "Reduced-order models for representing converters in power system studies," *IEEE Trans. Power Electron.*, vol. 33, no. 4, pp. 3644–3654, Apr. 2018.

[27] F. Cecati, M. Andresen, R. Zhu, Z. Zou, and M. Liserre, "Robustness analysis of voltage control strategies of smart transformer," in *Proc. 44th Annu. Conf. IEEE Ind. Electron. Soc.*, Oct. 2018, pp. 5566–5573.

[28] H. K. Khalil and J. W. Grizzle, *Nonlinear Systems*. Upper Saddle River, NJ, USA: Prentice-Hall, 2002.

[29] J. J. Grainger and W. D. Stevenson, *Power System Analysis*. New York, NY, USA: McGraw-Hill, 2003. [Online]. Available: https://www.mheducation.com/highered/product/power-system-analysis-grainger-stevenson/9780070612938.html

[30] F. B. Hildebrand, *Introduction to Numerical Analysis*. Chelmsford, MA, USA: Courier Corporation, 1987.

[31] G. F. Franklin, J. D. Powell, A. Emami-Naeini, and J. D. Powell, *Feedback Control of Dynamic Systems*. Reading, MA, USA: Addison-Wesley, 1994.
[32] A. Isidori, *Nonlinear Control Systems*. Berlin, Germany: Springer-Verlag, 1989.
[33] X. Wang, Y. W. Li, F. Blaabjerg, and P. C. Loh, "Virtual-impedance-based control for voltage-source and current-source converters," *IEEE Trans. Power Electron.*, vol. 30, no. 12, pp. 7019–7037, Dec. 2015.
[34] R. Teodorescu, M. Liserre, and P. Rodriguez, *Grid Converters for Photovoltaic and Wind Power Systems*. Hoboken, NJ, USA: Wiley, 2011.
[35] M. Cespedes and J. Sun, "Impedance modeling and analysis of grid-connected voltage-source converters," *IEEE Trans. Power Electron.*, vol. 29, no. 3, pp. 1254–1261, Mar. 2014.
[36] F. Wang, J. L. Duarte, M. A. M. Hendrix, and P. F. Ribeiro, "Modeling and analysis of grid harmonic distortion impact of aggregated DG inverters," *IEEE Trans. Power Electron.*, vol. 26, no. 3, pp. 786–797, Mar. 2011.
[37] J. Sun, "Impedance-based stability criterion for grid-connected inverters," *IEEE Trans. Power Electron.*, vol. 26, no. 11, pp. 3075–3078, Nov. 2011.

Federico Cecati (Student Member, IEEE) received the B.Sc. degree in ICT engineering and the M.Sc. degree in control engineering from the University of L'Aquila, L'Aquila, Italy, in 2015 and 2017, respectively.

Since 2018, he has been a Ph.D. Researcher with the Chair of Power Electronics, Kiel University, Kiel, Germany. From September 2020 to February 2021, he was a Guest Researcher with the Institute of Energy Technology, Aalborg University, Aalborg, Denmark. His research interests include modeling, stability analysis, and control of power electronics-based power systems and ancillary services in renewable energy systems.

Rongwu Zhu (Member, IEEE) received the B.Eng. degree in electrical engineering from Nanjing Normal University, Nanjing, China, in 2007, and the Ph.D. degree in energy technology from the Department of Energy Technology, Aalborg University, Aalborg, Denmark, in 2015.

From 2011 to 2012, he was a Guest Researcher with Aalborg University, and from 2015 to 2020, he was a Senior Researcher with the Chair of Power Electronics, Christian-Albrechts-University of Kiel, Kiel, Germany. He is currently a Full Professor with the Harbin Institute of Technology, Shenzhen, China. He has authored and coauthored more than 100 technical papers (more than 1/3 of them in international peer-reviewed journals/magazine), and six patents. His research interests include renewable power generation system, operation and control of electric grid with high penetration of renewables, and reliability and resilience improvement of power electronics dominated grid.

Dr. Zhu has served as a Guest Associate Editor for IEEE JOURNAL OF EMERGING AND SELECTED TOPICS IN POWER ELECTRONICS, a Guest Editor-in-Chief for *CSEE Journal of Power and Energy Systems*, an Editor for *International Transactions on Electrical Energy System*, an Associate Editor for IEEE OPEN JOURNAL OF POWER ELECTRONICS, and a Technical Committee Chair or Member of several international conferences.

Marco Liserre (Fellow, IEEE) received the M.Sc. and Ph.D. degree in electrical engineering from Bari Polytechnic, Bari, Italy, in 1998 and 2002, respectively.

He has been an Associate Professor with Bari Polytechnic, and from 2012, a Professor in reliable power electronics with Aalborg University, Aalborg, Denmark. From 2013, he is a Full Professor and holds the Chair of Power Electronics with Kiel University, Kiel, Germany. He has authored and coauthored 500 technical papers (1/3 of them in international peer-reviewed journals) and a book. These works have received more than 35 000 citations.

Dr. Liserre is listed in ISI Thomson report "The world's most influential scientific minds" from 2014. He has been awarded with an ERC Consolidator Grant for the project The Highly Efficient And Reliable smart Transformer (HEART), a new Heart for the Electric Distribution System. He is a Member of the IEEE Industry Applications Society (IAS), IEEE Power Electronics Society (PELS), IEEE Power and Energy Society (PES), and IEEE Industrial Electronics Society (IES). He has been serving all these societies in different capacities. He was the recipient of the IES 2009 Early Career Award; the IES 2011 Anthony J. Hornfeck Service Award; the 2014 Dr. Bimal Bose Energy Systems Award; the 2011 Industrial Electronics Magazine Best Paper Award in 2011 and 2020; the Third Prize paper award by the Industrial Power Converter Committee at ECCE 2012; 2012 and 2017 IEEE PELS Sustainable Energy Systems Technical Achievement Award; and the 2018 IEEE-IES Mittelmann Achievement Award.

Xiongfei Wang (Senior Member, IEEE) received the B.S. degree in electrical engineering from Yanshan University, Qinhuangdao, China, in 2006, the M.S. degree in electrical engineering from the Harbin Institute of Technology, Harbin, China, in 2008, and the Ph.D. degree in energy technology from Aalborg University, Aalborg, Denmark, in 2013.

Since 2009, he has been with the Department of Energy Technology, Aalborg University, where he became an Assistant Professor in 2014, an Associate Professor in 2016, and a Professor and Leader of Electronic Power Grid (eGRID) Research Group in 2018. He has also been a part-time Professor with the KTH Royal Institute of Technology, Stockholm, Sweden, since 2020. His current research interests include modeling and control of power electronic converters and systems, stability and power quality of power-electronics-dominated power systems, and high-power converters.

Dr. Wang serves as a Member-at-Large of Administrative Committee for the IEEE Power Electronics Society (PELS) in 2020–2022, a Co-Editor-in-Chief for IEEE TRANSACTIONS ON POWER ELECTRONICS, and as an Associate Editor for IEEE JOURNAL OF EMERGING AND SELECTED TOPICS IN POWER ELECTRONICS (JESTPE). He was selected into Aalborg University Strategic Talent Management Program in 2016. He was the recipient of six Prize Paper Awards in the IEEE Transactions and conferences, the 2018 Richard M. Bass Outstanding Young Power Electronics Engineer Award, the 2019 IEEE PELS Sustainable Energy Systems Technical Achievement Award, the 2020 IEEE Power and Energy Society Prize Paper Award, the 2020 JESTPE Star Associate Editor Award, and the Highly Cited Researcher in the Web of Science in 2019–2021.